Nuclear Materials and Energy 34 (2023) 101349

Contents lists available at ScienceDirect

Nuclear Materials and Energy

journal homepage: www.elsevier.com/locate/nme

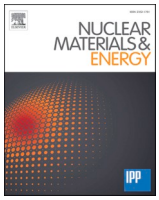

Optimisation of W_2B-W composites for radiation attenuation and thermal-mechanical performance

Samuel Humphry-Baker [a,*], Ouguzi Aihemaiti [a], Eugene Ivanov [b], Eduardo del Rio [b], Colin Windsor [c], Jack Astbury [c]

[a] Department of Materials, Imperial College London, London SW7 2BP, UK
[b] Tosoh SMD Inc, 3600 Gantz Rd., Grove City, OH 43123, USA
[c] 173 Brook Drive, Milton Park, Oxon OX14 4SD, UK

ARTICLE INFO

Keywords:
Neutron shielding
Tungsten borides
Composites
Thermophysical properties
Mechanical properties

ABSTRACT

The neutronics and engineering properties of a composite radiation shielding material, W_2B-W, are systematically investigated. Neutronics calculations using the MCNP code indicate that each additional 1 % volume fraction W_2B reduces the neutron energy flux into the superconducting core by 0.4–0.9 %, and reduces the gamma flux by 1.0–2.2 %, depending on the shield thickness. Materials with W_2B volume fractions of 43 and 89 % are fabricated by vacuum hot-pressing, resulting in a microstructure in which the dominant interpenetrating phase was W and W_2B respectively. For the W_2B-dominant material the thermophysical and mechanical properties were inferior. For example, room temperature flexural strength, fracture toughness, and thermal conductivity were all lower (by ~25%, 30% and 40% respectively). Also, the brittle to ductile transition temperature was ~500 °C higher. The results indicate that when considering boride content there is an important trade-off between shielding performance and thermal stress resistance.

1. Introduction

In compact fusion power plants the available space for neutron shielding will be minimal, therefore advanced materials are required [1,2]. Such advanced shielding is particularly needed on the in-board side of a spherical tokamak reactor, also known as the central column, which houses the superconducting magnets in a relatively compact structure. The magnets are highly sensitive to radiation damage [3,4] meaning their neutron exposure rate will determine their lifetime. Thinner shielding is also required to improve the device aspect ratio, leading to increased magnetic field strength in the plasma, and a corresponding improvement in fusion power density [5]. The shielding efficiency therefore controls both the longevity and performance of the device.

The shield must attenuate both neutrons and secondary gamma rays. For gamma attenuating applications like beam collimators and nuclear medicine, the attenuation efficiency increases with atomic number, therefore heavy alloys like tungsten are commonly employed [6]. Meanwhile, good neutron moderation requires low atomic number materials like graphite and water [7]. The opposing requirements for both light and heavy elements can be met through ceramic compounds and composites based on the transition metal hydrides [8] carbides [9], and borides [10,11]. In this study we will focus on the tungsten borides. Borides offer that added advantage of a high neutron capture cross section for the minor isotope B-10 below 1 keV, which occurs via the reaction $^{1}n + {}^{10}B \rightarrow {}^{7}Li + {}^{4}He$ [10]. Tungsten is selected due to its high mass density and atomic number, as well as its high cross section for (n, 2n) reactions in the range 10–20 MeV [10].

Monolithic tungsten boride ceramics are challenging to manufacture into bulk components due to their high melting points (2360–2670 °C) and sluggish diffusivities. For example, sintering of boride powders generally requires advanced techniques like spark plasma sintering [12], or hot-pressing at sintering temperatures in excess of 2000 °C to reach full density [13]. Sintering of fully dense materials at moderate temperatures therefore requires a second sintering aid. Typical metallic aids like Co [14], Al [15], and Fe [16,17] may not be appropriate as they can react to form brittle ternary intermetallic phases. Furthermore, such transition metals reduce shielding efficiency, and in the case of Co would lead to high activation and associated complications with reactor shut down and maintenance schemes.

* Corresponding author.
E-mail address: shumphry@ic.ac.uk (S. Humphry-Baker).

https://doi.org/10.1016/j.nme.2022.101349
Received 2 November 2022; Received in revised form 13 December 2022; Accepted 19 December 2022
Available online 20 December 2022

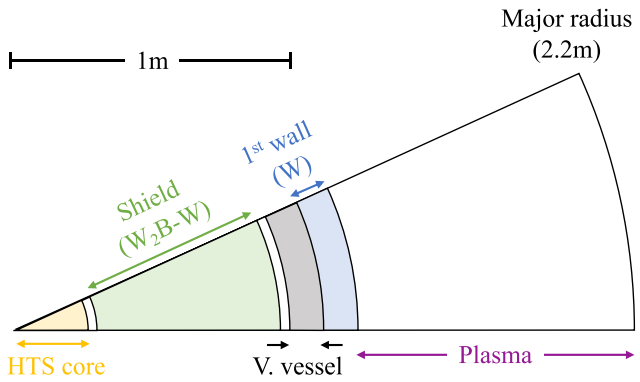

Fig. 1. Radial build of the largest tokamak shielding model (not to scale).

A secondary challenge relates to the hard and brittle nature of the tungsten borides [18–21]. Their microhardness is significantly higher than conventional shielding materials like metallic W (4.5 GPa [22]) and increases monotonically with boron content [18–21], from ~ 24 for W_2B [18] to 36–46 GPa for WB_4 [20,21]. Modelling suggests all five equilibrium phases including W_2B have a fracture toughness in the range 3 – 4.5 MPa $m^{1/2}$ [23,24], which is significantly lower than that for powder processed W, reported to be 8–28 MPa $m^{1/2}$ [25–27]. Experimental fracture toughness data is not yet available, nor is data on their thermomechanical properties. Tungsten boride thermophysical properties are also inferior to tungsten. Linear thermal expansion coefficient increases with increasing boron content, from ~ 6.7 to 7.8 x10^{-6} K^{-1} for W_2B and W_2B_5 respectively [28]. There are few studies on thermal conductivity; the room temperature value of the W_2B_5 phase is reported to be 52 $Wm^{-1}K^{-1}$ [28], however the effect of microstructure on conductivity is unknown.

These challenges associated with monolithic boride ceramics place an importance on developing new composite materials with enhanced performance. In previous works, we proposed a W_2B-W composite [29]. With a major fraction of W (~57 vol%), full density was achieved at a moderate sintering temperature of 1700 °C. The resulting properties were favourable compared to pure W: its high temperature strength was superior, and its oxidation resistance was also favourable, forming protective B_2O_3 scales that are stable up to 1000 °C [30]. However, W_2B was the minor phase, which will inevitably limit neutron shielding performance. It is therefore important to understand how the W_2B volume fraction affects shielding performance and thermal-mechanical properties.

In this paper we address these points through a combined experimental and simulations approach. We first perform neutronics simulations on various W_2B-W composites, which motivates the fabrication of a W_2B-W composite with approximately twice the W_2B content of previously studied materials in Ref. [29]. We then evaluate the thermophysical and mechanical properties of the two materials which enables their thermal-stress resistance to be compared.

2. Neutronics calculations

Neutron and photon transport calculations were performed using the code MCNP 6.2.0 [31]. The calculations follow the methods of a previous paper on pure tungsten boride ceramics, where further details can be found [10]. In summary, the cross-section libraries were FENDL 3.0 (neutron), MCPLIB84 (photon), and ENDF7U (photon-neutron). The weight windows were optimized for reducing the variance of low and epithermal energy neutrons and secondary gamma photons in the core's centre. Heat deposition tallies (type F6) were scored within the HTS core for neutrons and photons using the weight windows generated in the first stage calculation. Neutron-only transport models were run in MODE N with energy-resolved neutron flux tallies (type F4) using the CCFE-709 energy group scheme and the variance reduction from stage one turned on.

Table 1
Theoretical and practically achievable (98% theoretical) densities for the pure materials and for the six composite materials considered.

at. % B	Vol % W_2B	Theoretical density (g/cc)	98 % density (g/cc)
0	0	19.3	18.91
5	12.0	19.03	18.65
10	24.9	18.75	18.37
15	38.8	18.44	18.07
20	53.8	18.11	17.75
25	69.9	17.75	17.40
30	87.5	17.37	17.02
33.3	100	17.09	16.75

The energy depositions were computed for a nominal 200 MW fusion power plant. The fusion neutron creation matrix consisted of 68 radial segments and 200 vertical segments, as provided from the Tokamak Energy System Code. The results reported here correspond to the integrated energies, and to the vertical mid-plane section within +/- 200 mm of the vertical shield centre. Five tokamak major radii were considered: 1.2, 1.4, 1.6, 1.8, 2.0, and 2.2 m. For each device, the superconducting core radius and metallic tungsten first wall were kept constant at 250.9 mm and 40 mm respectively. Meanwhile, the shield thickness was adjusted to keep the plasma gap between the inner plasma boundary and the first wall constant. This gave 5 shield thicknesses between 253 and 670 mm. Fig. 1 illustrates the radial build of the largest model.

Six composite shielding materials were considered, with atomic boron contents of 5, 10, 15, 20, 25, and 30 at. %, in addition to pure W and pure W_2B (i.e., 0 and 33.3 at. %). The corresponding modelled densities of the materials are shown in Table 1. The volume fraction of W_2B was calculated using the average atomic masses of pure W (183.84 g mol^{-1}) and W_2B (126.14 g mol^{-1}), and using theoretical densities for the constituent phases of 19.3 and 17.09 g/cc respectively [28]. From this, the theoretical composite density (i.e. the density in the absence of any porosity) was calculated using a rule of mixtures. The density used in the shielding calculations was taken to be 98 % of this value, to account for some inevitable residual porosity after sintering. This value was used following previous experimental results on W_2B-W [29] and to be consistent with shielding results reported in Ref. [10] for the pure tungsten boride materials.

Fig. 2 shows the integrated energy deposition into the central superconducting core; the results are separated by gamma rays (left) and neutrons (right). Energy deposition is plotted as a function of the W_2B volume fraction. The results for the pure W and W_2B, taken from Ref. [10] are also shown for comparison. Results for several device major radii are shown between $R_0 = 1.4$ m and $R_0 = 2.2$ m. In all cases the gamma energy deposition is about an order of magnitude larger than the neutron energy, which is consistent with results seen on other tungsten boride phases [10]. For the composite materials, the energy deposition for both neutrons and gammas generally decreases exponentially with increasing boride fraction. For the gammas, the rate of decrease is higher. For example, at $R_0 = 2.0$ m, the power deposition falls by a factor of 10 between 0 and 33 at. % B. While for the neutrons, the corresponding fall is by only a factor of 2.5.

For the thinner shields, the composite materials are consistent with the pure W and pure W_2B materials, showing a continuous exponential trend. However, for the thicker (i.e., reactor relevant) shields, there appears to be some curvature in the data, i.e. a greater than expected decrease between 0 and 5 at. % B and a flattening of the trend between 25 and 33 at. % B. This point requires further analysis to understand its origins.

It should be noted that the best performing W_2B-W shields are not as efficient at attenuating radiation as the compound W_2B_5. For example, at $R_0 = 2.2$ m, the total power deposition for the 87.5 vol% W_2B composite

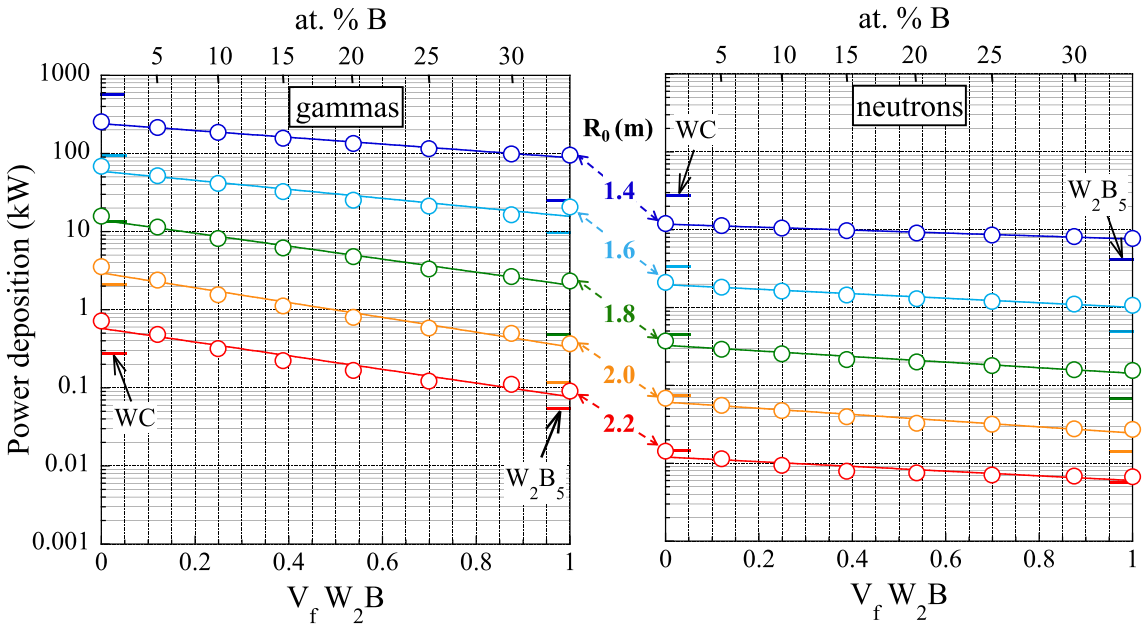

Fig. 2. The energy deposition from (a) gammas and (b) neutrons into the HTS core for W_2B-W shields of varying volume fraction boride phase, for the five major tokamak radii considered. The slopes of the exponential fits varied in the range 1.0–2.2 for the gammas and 0.4–0.9 for the neutrons. Data for the monolithic ceramics WC and W_2B_5 are shown by line dashes.

is 0.129 kW, while for W_2B_5 it was almost a factor of 3 lower, at 0.046 kW [10]. However, the W_2B-W shields still outperform other materials such as WC and cemented tungsten borocarbides [10]; as the corresponding power depositions for these materials under identical conditions were 0.36 and 0.3 kW respectively [10]. The full data sets for the monolithic ceramics WC and W_2B_5 from Ref. [10] are provided for comparison, as shown by line dashes to the far-left and far-right of each figure part respectively.

3. Experimental methods

3.1. Sample preparation and characterisation

The W_2B-W materials were hot pressed from powder mixtures of pure tungsten metal (<15 μm, 99.999 % purity) and boron nitride (9–12 μm, 99.9 % purity) under vacuum condition ($<10^{-5}$ Torr), in a graphite die. Two nominal compositions were studied: 1.27 and 2.8 wt% B, corresponding to 16 and 30 at.%. However, the real boron concentration may be somewhat lower due to boron evaporation during sintering. Hereafter these materials are referred to as W-16B and W-30B. The materials were sintered at 1700 °C and 2025 °C respectively. Further details on W-16B fabrication can be found in our previous study [29]. After sintering the surface was ground using a high-speed SiC wheel to remove ~ 1 mm of tungsten carbide layer formed during the reaction with the graphite die. The ground billet was then cut with electrical discharge machining (EDM) into test samples.

Samples were prepared for characterisation in the following sequence: silicon carbide papers to a 45 μm finish; diamond impregnated discs to 5 μm; and finally diamond suspensions to 1 μm. X-ray diffraction (XRD) was performed in spinning mode on a Bruker D2 desktop diffractometer, from 20 to 90°2θ, at 2° min^{-1}. A copper X-ray source (λ = 0.154 nm) was used. The as-sintered samples were imaged with a Zeiss Sigma 300 Scanning Electron Microscope (SEM) in Back-Scattered Electron mode under a 10 kV voltage and using Electron backscatter diffraction (EBSD) at 20 kV. The grain size was analysed via the linear intercept method on at least 200 grains per sample. Phase volume fractions were determined with Image J software: the already identified phase regions from EBSD were manually outlined and the enclosed pixel counts were recorded for each phase. The same method was used to calculate porosity. The relative density was determined using the Archimedes method.

3.2. Mechanical properties

The hardness was measured using a Vickers diamond indenter on samples polished to a 1 μm finish. Samples were indented at loads of 1, 3, 5, 10, 20, and 30 kg, with 5 identical indents at each load. The hardness was calculated using the formula: $HV = 0.1891P/d^2$, where P is the load force and d was the indent diagonal, which was imaged with a JSM-6010LA SEM at 20 kV, in Secondary Electron Imaging mode.

Three-point flexural tests were performed to determine strength and plane strain fracture toughness, K_{1C}. (NB: conventional tensile tests could not be performed due to difficulties in gripping the samples, which is associated with their low strain to failure). For both tests, samples of were cut to the dimensions 3 × 4 × 25 mm and polished to a 15 μm finish. The exact dimensions were measured with a digital micrometre, of precision 1 μm, at the centre of the cross section. Loading was conducted on a 10kN Zwick Roell Z010 in compression mode with three-point fixtures with a load span, S, of 20 mm. Four specimens were loaded for each composition at a constant crosshead speed was 0.5 mm min^{-1}. The strength was measured using the formula:

$$\sigma_{flexural} = \frac{3SP_{max}}{2tw^2} \quad (1)$$

where P_{max} is the maximum load in the load–deflection curve, t is the specimen width (~3mm), and w is the specimen depth (~4mm). For the K_{1C} experiments, specimens were notched in the Single Edge Notched Beam (SENB) configuration in the EDM, giving an initial notch radius of 0.15 mm, which was then sharpened using a reciprocating razor blade machine and 1 μm diamond suspension to a notch radius of ~ 20 μm. The final notch depth was measured in the SEM on both sides of each beam and the average taken. K_{1C} was calculated using the formula [32]:

$$K_{1C} = \frac{P_i S}{tw^{\frac{3}{2}}} f\left(\frac{a}{w}\right) \quad (2)$$

where Pi is the load where cracking first initiates (taken at the point a deviation from linearity in the load–deflection curve is observed), a is

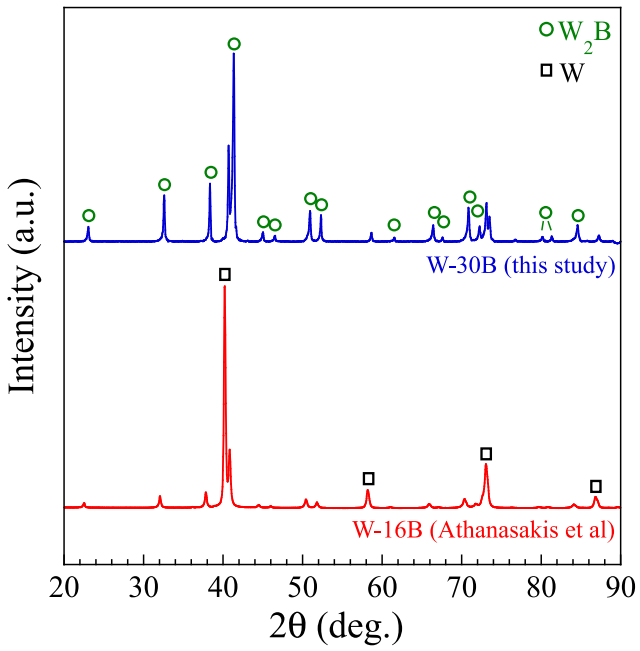

Fig. 3. X-ray diffraction pattern of W-30B (blue) compared to data for W-16B from Ref. [29], with corresponding peaks labelled for W (black squares) and W_2B (green circles). (For interpretation of the references to colour in this figure legend, the reader is referred to the web version of this article.)

the crack height, and f(a/w) is given by [32]:

$$f\left(\frac{a}{w}\right) = 3\sqrt{\frac{a}{w}}\,\frac{1.99 - \frac{a}{w}\left(1-\frac{a}{w}\right)\left[2.15 - \frac{3.93a}{w} + 2.7\left(\frac{a}{w}\right)^2\right]}{2\left(1+\frac{2a}{w}\right)\left(1-\frac{a}{w}\right)^{\frac{3}{2}}} \quad (3)$$

Flexural strength tests were also performed at high temperature using an Instron universal testing machine in vacuum with graphite pushrods from 500 °C to 1700 °C at 200 °C increments, with three tests at each temperature. Further details can be found in a previous report [29]. The load separation, *S*, was 18–20 mm for the high temperature tests. The larger separation was used around the temperature range where the flexural strength exceeded 1 GPa, to prevent damaging the graphite fixtures. Fracture surfaces were imaged using the same conditions as the hardness indents.

3.3. Thermal properties

Thermal diffusivity was measured using a Netzsch LFA 427 laser flash analyser with an alumina sample holder. Samples were disk shaped, with 12.7 mm diameter and 3–4 mm thickness. The surfaces were coated with graphite to reduce surface reflectivity. Measurements were taken at 100 °C intervals from 25 to 600 °C, and in 200 °C intervals from 600 to 1400 °C. At each set-point temperature the measurement was repeated 3 times. All measurements were performed in flowing helium. The laser voltage was 600 V and the pulse lasted 0.8 ms. The pulse duration and heat losses were corrected for using the Cowan method [16].

Specific heat capacity was measured using a Netzsch STA 449 F1 Jupiter Differential Scanning Calorimeter (DSC) with a platinum sensor and platinum crucibles. The purge gas was argon flowed at 20 ml/min. The standard ratio method was used (ISO 11357–4) with a sapphire disk of 60 mg and sample mas of ~ 400 mg such that total heat flow of the sample and standard were approximately the same. The heating rate was 20 K/min between 50 and 1200 °C, with a 10-minute isothermal hold before and after the heating stage. Datapoints at 100 °C intervals were extracted based on the average heat flow within 50 °C of each interval temperature.

Thermal expansion was measured using a Netzsch 402DIL dilatometer. Cuboidal samples of 4 × 4 × 25 mm were loaded into a graphite pushrod assembly with a compressive force of 75 mN. Samples were heated at 10 K/min to 1300 °C in helium. Instrument thermal expansion was corrected for using a 25 mm graphite standard. Thermal expansion coefficients were calculated at intervals of 100 °C by averaging the thermal expansion from 50 °C below to 50 °C above the interval. The procedure was repeated for two nominally identical samples, and the

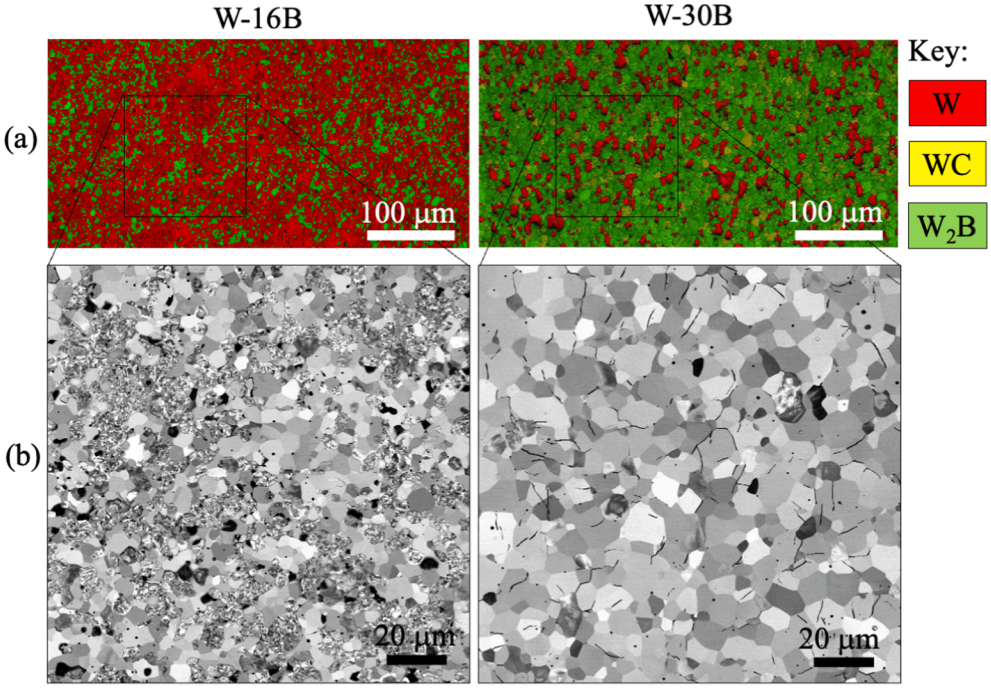

Fig. 4. A comparison of the as-received samples, W-16B and W-30B, showing (a) EBSD phase maps, revealing the different boride phase fractions of ~ 43 % and ~ 89 %; (b) SEM images in BSE mode revealing the increase in grain size from 5 to 10 µm, and the structure within the W regions.

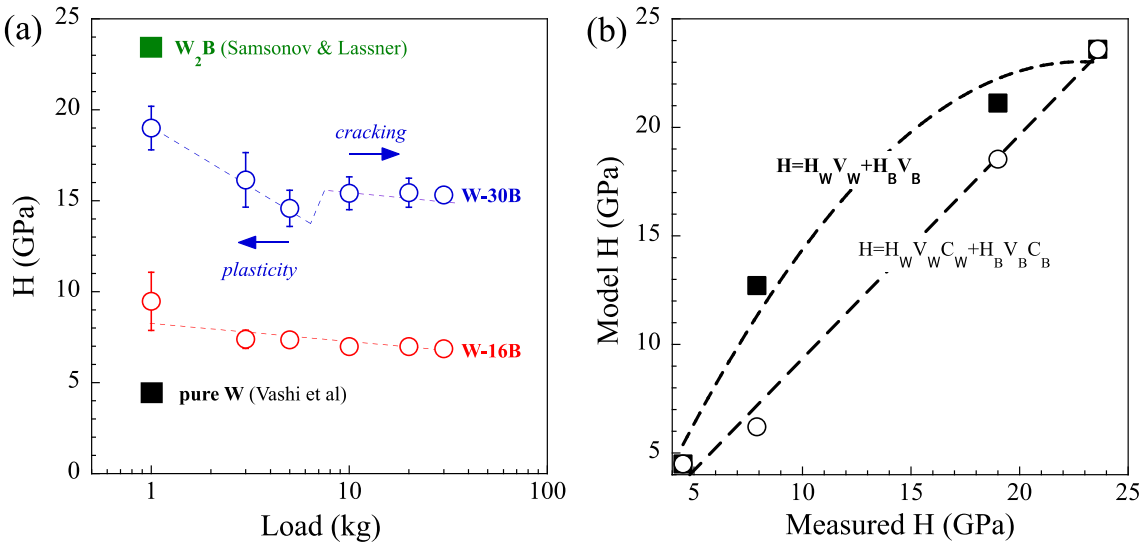

Fig. 5. (a) Vickers indentation hardness of W-30B, W-16B vs applied load. Error bars indicate standard deviation of five hardness measurements at each load. Hardness of pure W [22], and W_2B [18,35] (b) Model hardness vs experimental hardness for two hardness models: (i) rule of mixtures (bold squares); (ii) and a modified rule of mixtures including phase contiguity (open circles). The contiguity model fits the data well.

average taken.

4. Experimental results and discussion

4.1. Microstructural characterisation

The X-ray data in Fig. 3 indicates that W-30B is a two-phase composite made up exclusively from BCC metallic W phase and tetragonal W_2B phase. The obtained peaks match well with ICDD card (refs 004–0806 and 025–0990). The lattice parameters were 0.318 nm for W, and a = b = 0.559 nm, c = 0.477 nm for W_2B. These parameters are slightly larger than the values reported in Ref. [29] for W-16B, which were 0.317 nm for W, and a = b = 0.558 nm, c = 0.475 nm. Both values are within 0.003 nm of the reference values (0.316 nm for W, and a = b = 0.557 nm, c = 0.474 nm for W_2B).

Fig. 4 shows the microstructures of the W-16B and W-30B samples in more detail. Part (a) shows the phase map from EBSD, with the W phase in red and the W_2B phase in green. There is a clear change in morphology: in W-16B, the W_2B phase forms loosely connected particles in a continuous W matrix; while in W-30B, the W_2B phase forms a continuous matrix, with isolated W domains. In W-30B there was also a small number of WC particles (shown in yellow), due to carbon contamination from the graphite dies, however the volume fraction was not significant.

Part (b) shows magnified BSE-SEM images, revealing the grain morphologies and porosity. The grains of the boride phase were equiaxed and normally distributed in both cases and had an average size of 3.1 and 6.1 μm for W-16B and W-30B respectively. The higher grain size in W-30B is likely due to the 325 °C higher sintering temperature. The metallic W domains appeared to consist of multiple grains, although the grain size could not be reliably quantified.

The volume fraction of the W_2B phase was 43 and 89 vol% respectively. In comparison, volume fractions predicted with the lever rule are 54 and 91 vol%. The slightly lower experimental values cannot be due to dissolution of boron in tungsten, as its solubility for boron is<0.25 at.% [33]. It is likely that some boron reacted with oxygen impurities in the material and subsequently evaporated, since B_2O_3 is volatile at high temperature. The Archimedes densities of W-16B and W-30B were 17.8 and 17.1 g/cc respectively, which are 97 and 98.6 % of theoretical density respectively. The values are in reasonable agreement with the porosity obtained with Image J pixel analysis, which were 1.1 and 1.2 %.

The microcracks observed in Fig. 4(b) for W-30B are interpreted to be induced during the surface preparation, as it was found that more aggressive grinding (e.g., faster wheel speed) tended to induce extensive grain pull-out.

4.2. Room temperature mechanical properties

Fig. 5(a) shows the Vickers hardness of W-30B and W-16B with respect to indentation load. At all loads studied, the higher boron content resulted in greater hardness. For example, at 30 kg, the hardness of W-30B was 15.4 ± 0.4 GPa, while W-16B had a hardness of 6.9 ± 0.1 GPa. The repeatability of the measurement, indicated by the standard deviation on 5 indents, was generally < 10 % of the hardness value. However, for W-16B at 1 kg load, the standard deviation was slightly greater. This was because the indent diagonal at this load was only 10 μm, which was comparable to the size of the W_2B domains, therefore the W_2B volume fraction was not consistent around each impression.

Both materials show a clear indentation size effect, with the hardness generally decreasing logarithmically with increasing load. E.g., from 1 to 5 kg, the hardness of W-30B dropped ~ 3.6 GPa while that for W-16B dropped ~ 2.5 GPa. For both materials the hardness data plateaus beyond 10 kg. For W-30B there was also a reverse indentation size effect between 5 and 10 kg, where the hardness increased slightly. The hardness increase was accompanied by the onset of large cracks emerging from the indent diagonals. The reverse size effect induced by cracking is described in more detail in Ref. [34]. There was no reverse hardness size effect in W-16B due to the absence of corner cracking.

Also shown on Fig. 5 are the 0.5–1 kg experimental microhardness of pure W [22] and pure W_2B [18,35]. The W_2B datapoint is the average of two studies (23.1 GPa [35] and 23.7 GPa [18]). Not shown on the plot are two other computational reports of microhardness (12.1 [24] and 15.1 [23]). The computation results deviate significantly from the experimental values, likely because they rely on empirically derived relationships between hardness and the shear modulus, which have no mechanistic basis.

Fig. 5(b) clarifies the effect of boride volume fraction on hardness further by plotting the experimental 1 kg microhardness values against those predicted from two literature models. The two models are the standard Rule Of Mixtures (ROM):

$$H = H_W V_W + H_B V_B$$

Table 2
Microstructural characteristics of the materials. Uncertainty in grain size is the maximum deviation when the population of analysed grains is halved. Theoretical densities for constituent phases are 19.3 g/cc for W and 17.09 g/cc for W_2B.

Composition	W_2B volume fraction	W_2B grain size (μm)	W_2B contiguity	Theoretical density (g/cc)	Archimedes density (g/cc)	Relative density (%)	porosity
W-16B	43	3.1 ± 0.1	0.48	18.3	17.8	97	1.1
W-30B	89	6.1 ± 0.2	0.90	17.3	17.1	98.6	1.2

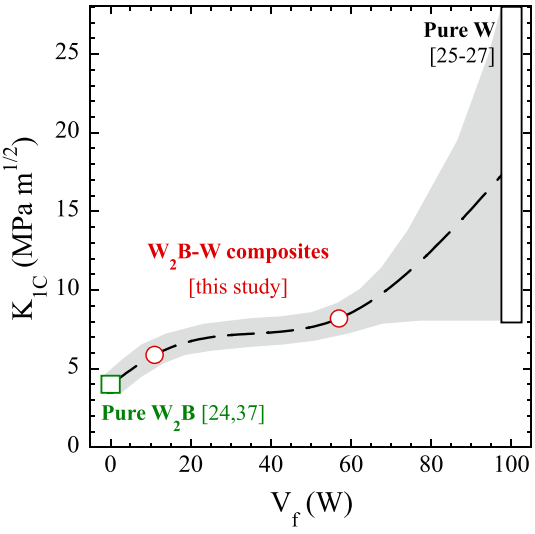

Fig. 6. The plane strain fracture toughness of W_2B-W composites (red) vs computational literature data for pure W_2B [24,37] (green) and K_{1C} values for pure W [25–27] (black). The standard deviation in W_2B-W K_{1C} data is smaller than the symbol size. Dotted line drawn through the W_2B-W experimental data and the bisect of the literature data extremities serves as a guide for the eye only. (For interpretation of the references to colour in this figure legend, the reader is referred to the web version of this article.)

and a ROM expression modified by the contiguity of each phase, as proposed by Lee and Gurland [36]:

$$H = H_W V_W C_W + H_B V_B C_B$$

In both expressions the hardness of W and W_2B, H_W and H_B, are taken as 4.5 GPa [22] and 23.6 GPa [18,35] respectively. The volume fractions, V_W and V_B, and contiguities, C_W and C_B, of each phase are taken from Table 2.

The ROM model (filled squares) overestimates the hardness, particularly in the case of W-16B, where the difference is about 5 GPa. This is likely because in W-16B, the W_2B particles are not well connected to each other, with a contiguity of only 48 %, and are therefore the composite is able to deform with minimal plasticity in W_2B. When the contiguity-modified ROM, a near linear 1:1 relationship is found.

The results for the plane strain fracture toughness (K_{1C}) are shown in Fig. 6. K_{1C} for the W-16B composite was 8.2 ± 0.2 MPa $m^{1/2}$ and that for W-30B composite was 5.9 ± 0.4 MPa $m^{1/2}$. These values are significantly higher than available computationally predicted values for W_2B, which vary between 3.5 [24] and 4.5 MPa $m^{1/2}$ [37] the average of which is shown as a green square in Fig. 6. We note that the W_2B computational results may again not be accurate as they emanate from empirical relations between elastic moduli and toughness, derived from other ceramics, the majority of which are not metal borides. However the predicted values do align well with experimentally determined values for other metal borides such as ZrB_2 (2.5–4.2 MPa $m^{1/2}$ [38]) and HfB_2 (4.1 MPa $m^{1/2}$ [39]). Data for powder processed pure W is shown as a black rectangle, covering the range of 8–28 MPa $m^{1/2}$ [25–27]. The 50% higher toughness in W-30B vs pure W_2B suggests that the presence of only a small volume fraction of W (~10 vol%) improves the toughness significantly. Such toughening improvement suggests good interfacial bond strength between W and W_2B. This is supported by recent qualitative measurements (based on Rockwell C indentation test) of coating adhesion between W_2B coatings and W substrates [40]. However more detailed delamination tests are needed to properly quantify the W_2B-W bond strength.

4.3. Thermomechanical properties

Fig. 7 shows the high temperature flexural strength of W-30B. Part (a) contains the typical raw stress-displacement traces, showing that the samples fractured in a brittle manner with an increasing failure stress up to 1500 °C. Up to 900 °C this increase was minor, but between 900 °C and 1500 °C the increase was significant. Above 1700 °C the samples then became ductile, and the failure stress decreased.

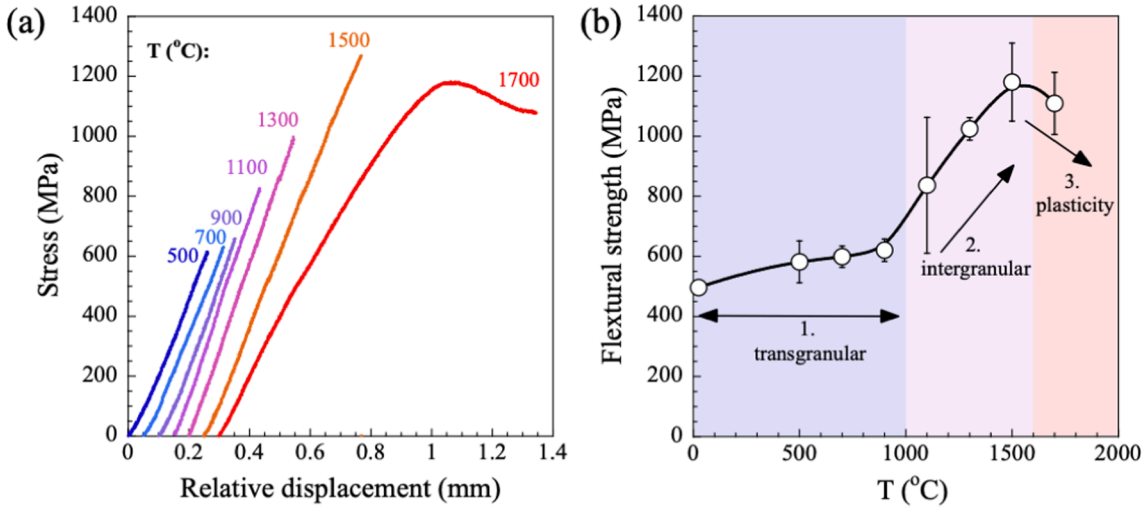

Fig. 7. High temperature flexural strength of W-30B; (a) typical stress-displacement curves; (b) average flexural strength as a function of temperature. Error bars indicate the standard deviation between 3 nominally identical tests.

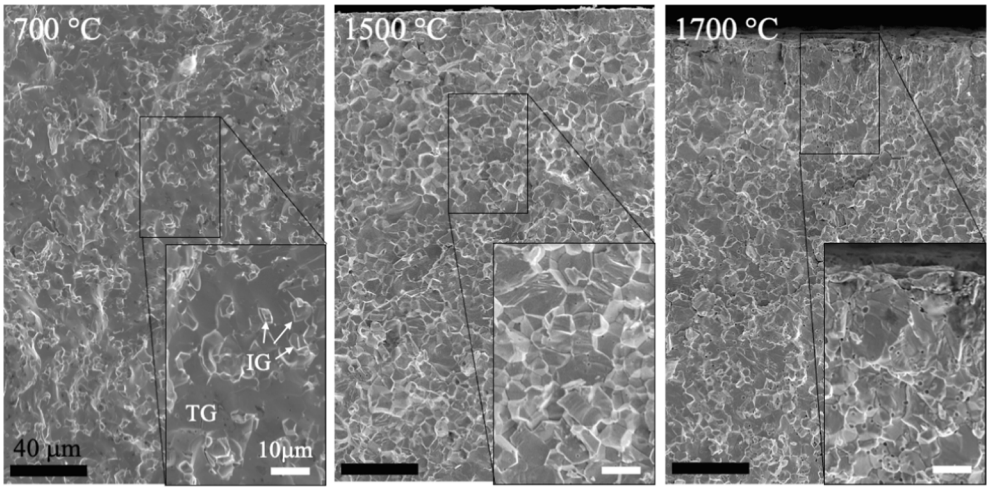

Fig. 8. SEM fracture surfaces of W-30B specimens near tensile surface (upper side) at 700, 1500, and 1700 °C. At 700 °C, transgranular and intergranular cracks are labelled in the inset as TG and IG, respectively. At 1700 °C, inset shows a plastic zone near the tensile surface with increased void formation.

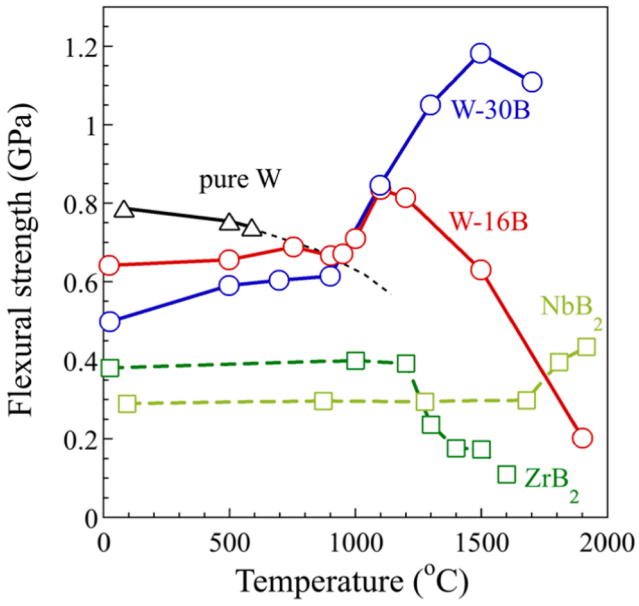

Fig. 9. (a) High temperature flexural strength of W-30B, W-16B [29], pure W [41], NbB_2 [43], and ZrB_2 [44].

These three regimes of behaviour are shown more clearly in part (b), which plots the average flexural strengths from the three separate tests. The strength in each regime was as follows: (i) From 25 to 900 °C, the value was relatively insensitive to temperature, increasing marginally from 500 to 600 MPa; (ii) from 900 to 1500 °C, it rose more sharply, reaching a peak of 1180 MPa at 1500 °C; and finally (iii) between 1500 and 1700 there was a slight drop to in strength as the samples became ductile.

The fracture surfaces of the specimens in Fig. 8 illustrate the physical origin of the 3 regimes. For consistency, the specimens shown are those that exhibited the highest strengths. The micrographs are oriented such that the surface of maximum tensile stress is on the top side of the figure. The fracture morphology at 700 °C (left), was predominantly transgranular. A relatively smooth surface is seen across most of the sample, with small 5–10 μm protrusions of intergranular fracture. Their size, area fraction, and morphology suggest the protrusions are W grains. Similar surfaces were observed in all samples tested up to 900 °C.

At 1500 °C, shown in the middle section, the fracture surfaces were predominantly intergranular, as evidenced by the increasing dominance of grain edges. Intergranular cracking was observed in all samples tested at 1100 °C and above. Between 1100 and 1500 °C, the morphology became increasingly intergranular.

At 1700 °C, the surface remained mostly intergranular, however at the tensile surface there was a region that showed plastic deformation had occurred, as evidenced by the lack of grain contours, and some striated regions, indicative of dislocation slip. There was also an increased number of voids or cavities, which suggest the operation of creep-type deformation mechanism.

The first point of discussion regarding the flexural tests is the effect of boron content on the room temperature strength. For this we compare in Fig. 9 the results of this study with previous results on low boron W-16B [29] and pure W [41]. There is a clear monotonic decrease in room temperature strength with increasing boron content, decreasing from about 800 to 500 MPa from 0 to 30 at.% B. At low temperature, the strength of W-16B and W-30B were both controlled by brittle fracture, as evidenced by Fig. 6 (and similar micrographs in Ref. [29]). During brittle fracture, the strength is limited by the material's fracture toughness and the size of defects, such as pores or microcracks. While there is no evidence for any change in pore size, the fracture toughness of the W_2B phase (predicted to be 3.5–4.5 MPa $m^{1/2}$ [24,37]) is significantly lower than the W phase (experimentally determined to be 8–28 MPa $m^{1/2}$ [25,26,42]). Thus, a continual decrease in strength with increasing boride fraction is to be expected.

The second point of discussion is the brittle-to-ductile transition temperature. In W-16B [29] this temperature occurred between 1000 and 1100 °C, which was similar to recrystallised W [45] (although it is important to note the transition temperature in pure W can be markedly decreased through thermomechanical processing [46]). Whereas in W-30B, the transition occurred at around 1500 °C. The reason for this is likely the absence of a continuous network of metallic tungsten in the W-30B material, since the W grains were isolated (Fig. 4). This means that the W phase cannot accommodate significant deformation on the macroscale, therefore ductility is only possible when the W_2B phase also becomes ductile. The homologous temperature of W_2B phase ductilisation observed here (0.6 T_m) is similar to that of other transition metal borides [43,47]. For example, in ZrB_2 a peak in strength and onset of creep occur at 0.59 T_m (1800 °C) [47] and in NbB_2 a similar peak in strength is observed at 0.65 T_m (1900 °C), with creep induced cavities being observed when tested above 1700 °C [43].

The changes in strength with temperature for each W_2B-W material can therefore be interpreted as follows:

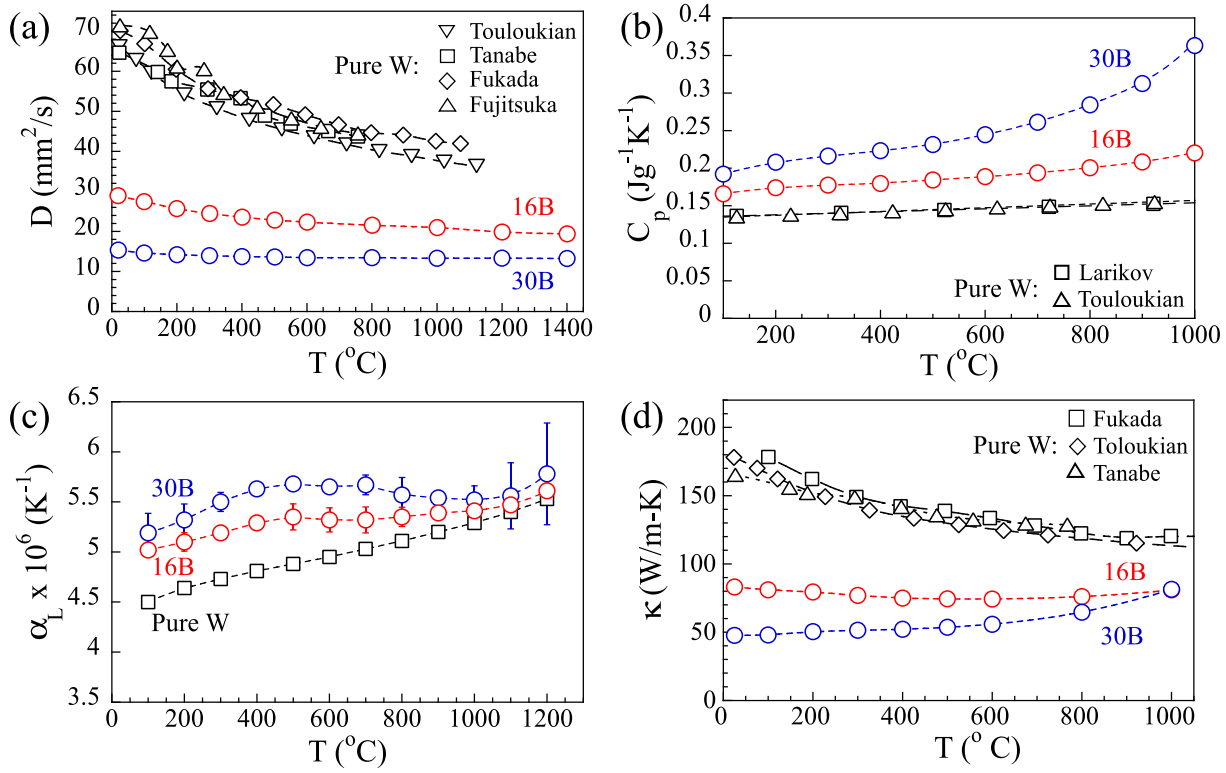

Fig. 10. Thermophysical properties of the W_2B-W composites compared to literature data for pure W: (a) thermal diffusivity, D [48–51]; (b) specific heat capacity, c_p [48,52]; (c) linear thermal expansion coefficient, α_L; and (d) thermal conductivity, κ [48–50].

1) W-16B (continuous W phase): the flexural strength remains constant with temperature initially, despite a softening of W phase, because the W_2B particles provide an Orowan-type strengthening mechanism. At ~ 1000 °C, the strength increases due to an increase in the toughness of the W phase, as evidenced by ductile cavitation in the W phase regions by Ref [29], and the known increase in toughness in pure W. For example, Mutoh et al showed a monotonic increase in K_{1c} of pure W from 15 to 39 MPa $m^{1/2}$ in the temperature range 20–800 °C [25]. Above ~ 1200 °C the strength then decreases due to a creep-type deformation in W.
2) W-30B (isolated W phase): again, the flexural strength begins to rise significantly at ~ 1000 °C due to the toughening in W. However, the accompanying softening of W does not lead to a drop in strength, because it remains as isolated particles, and the W_2B forms a continuous network. The strength therefore continues to rise until 1500 °C at which point the W_2B phase becomes ductile and deforms plastically.

4.4. Thermophysical properties

Fig. 10 shows the thermophysical properties of the W_2B-W composites from 25 to 1400 °C: (a) thermal diffusivity, D; (b) specific heat capacity, c_p; (c) linear thermal expansion coefficient, α_L; and (d) thermal conductivity, κ. The available literature data for pure W is also shown. Temperature dependant data for W_2B ceramics is not available.

The diffusivity values shown in part (a) decrease with increasing W_2B content. This is expected based on the partially covalent bonding character in the W_2B phase and the strong mass difference between B and W atoms. D of W-16B and W-30B is about is about 40–50 % and 20–30 % that of pure W, depending on the test temperature.

By comparison, the specific heat capacity shown in part (b) increases with increasing W_2B content, from 0.134 $Jg^{-1}K^{-1}$ for pure W, to 0.161 and 0.182 $Jg^{-1}K^{-1}$ for W-16B and W-30B, due to the higher atomic packing density in W_2B vs pure W [10]. The room temperature value for c_p of W-30B is identical to the literature values for pure W_2B 0.182 $Jg^{-1}K^{-1}$ [53].

Thermal expansion coefficients shown in part (c) also increase with increasing W_2B content. Unlike the c_p data, the thermal expansion of W-30B does not approach the literature value for pure W_2B, which was given as 6.7 $x10^{-6}$ K^{-1} in Ref. [28]. It is interesting to note that above 1000 °C or so the thermal expansion of the W_2B-W composites and pure W begin to converge. This may be related to the thermal expansion mismatch between the two phases, which would lead to compressive thermal stresses in the W_2B phase being gradually released as the temperature increases.

Finally, part (d) shows the thermal conductivity, as calculated using the equation: $\kappa = D\ c_p\ \rho$. The temperature dependent density, ρ, was calculated based on the room temperature Archimedes densities given in Table 2, and the temperature-dependant thermal expansion coefficients. As a room temperature c_p value was not available, it was estimated by fitting a second order polynomial to the temperature dependent data in the range 100–500 °C. The κ data shows a clear decrease with increasing W_2B content from 165 to 178 $Wm^{-1}K^{-1}$ for pure W to 83 and 48 $Wm^{-1}K^{-1}$ for W-16B and W-30B.

The significance of the thermal–mechanical data can be considered using the thermal stress resistance parameters. In the case of a hollow cylinder undergoing radial heat flow, for which the figure of merit for maximum allowable temperature difference across the cylinder wall is given by [54]:

$$R = \frac{\sigma_t(1-\nu)}{\alpha E} \tag{4}$$

and the maximum allowable heat flux through the wall is:

$$R' = \frac{\sigma_t(1-\nu)\kappa}{\alpha E} \tag{5}$$

where σ_t is the tensile strength, E is the Young's modulus, ν is the Poisson's ratio. Since temperature dependent elasticity data are not

Table 3
Thermal stress resistance of the materials from Eq. (4)-(5) compared to literature data on tungsten. Values for energy deposition (q) taken from the 2.2 m reactor model data in Fig. 2.

Composition	σ_t (MPa)	κ ($Wm^{-1}K^{-1}$)	α (10^{-6} K^{-1})	ν	E_y (GPa)	R (K)	R' (kW/m)	q (W)
pure W	790	170	4.5	0.28	410	308	52	732
W-16B	640	83.1	5.2	0.28	418	212	18	165
W-30B	500	47.7	5.0	0.29	428	166	7.9	67.2

available for W_2B, we use room temperature values only. E and ν of W are given as 410 GPa and 0.28 respectively, and those of W_2B are taken to be 430 GPa and 0.29 respectively, based on averages taken from Refs. [55–58]. For the prediction of E in the composites, we use the analytical expressive given by Paul [59]. Since the values of ν are very similar for W (0.28) and W_2B (0.29), the value of each composite is taken to be that of the dominant phase.

In Table 3, R and R' are given alongside the overall power deposition (q) from neutrons and gammas in the 2.2 m reactor model. The data for W is extracted directly from Fig. 2, and for the composite materials values have been calculated from the exponential line of best fit. The data suggests a trade-off between properties when increasing the boride content within the shield: although the power deposition onto the central column improves by a factor of 10 or so from pure W to W-30B, the thermal stress resistance parameter R decreases by a factor of $\sim$ 2 and the R' value decreases by a factor of $\sim$ 7. It should be added that while the thermal stress resistance is likely to degrade with increasing temperature for pure W – mainly due to the degradation in fracture strength (Fig. 9) – it is likely to improve with temperature for the boride containing materials, particularly W-30B, due to a corresponding improvement in these parameters. Temperature dependent stiffness data is needed to quantify this effect.

The trade-off between thermal–mechanical and attenuation performance suggests that for the shield composition to be optimised, the inter-relation of these properties must be properly understood. For example, the shield's mechanical performance will dictate the amount of structural support required from surrounding structural assemblies. Thus, if the mechanical properties improve, less structural material is required, which in turn increases the available space for shielding. Furthermore, the shield's thermal performance dictates the spacing of cooling channels, and the rate of coolant circulation required. Thus, better thermal performance will reduce the space required for coolant systems, which again increases the available space of shielding. For the trade-off in these factors to be properly quantified, a shielding figure of merit involving all parameters must be developed.

5. Conclusions

The effect of boron content in W_2B-W composites has been examined by combining neutronics simulations with experimental characterisation of thermal–mechanical properties. The shielding performance was found to improve with increasing boron content, while the thermal stress resistance of the material degraded. The main conclusions are as follows:

The neutronics simulations indicate that every additional 1 vol% W_2B in the composite reduces the neutron flux into the superconducting core by 0.4–0.9 %, and reduces the gamma flux by 1.0–2.2 %, depending on the device size.

A fully dense composite with a major volume fraction of W_2B phase (89 vol%), was achieved for the first time by increasing the sintering temperature from 1700 to 2025 °C. The continuous matrix phase was W_2B (W_2B-dominant), which provided an opposing microstructure to the 43 % W_2B volume fraction composite developed previously in which the continuous matrix phase was W (W-dominant).

The hardness of the W_2B-dominant composite was approximately double that of the W-dominant material and exhibited a reverse indentation size effect due to corner cracking at larger indentation loads. In the microhardness regime, i.e. in the absence of such cracking, data for both materials can be well fit with a contiguity-modified rule of mixtures.

The plane strain fracture toughness K_{1C} of both materials was found to be 5.9 and 8.2 MPa-$m^{1/2}$ for the W_2B-dominant and W-dominant materials respectively, which are $\sim$ 50 % and 100 % higher than the available data for pure W_2B. Room temperature flexural strength of the W_2B-dominant composite was degraded compared to W-dominant one and pure W, however the strength of both materials increased with temperature up to the softening point of the majority phase, which for the W-dominant material was 1000 °C and for the W_2B-dominant one was $\sim$ 1500 °C.

The thermal conductivity degrades with increasing boride fraction, from 83 and 48 $Wm^{-1}K^{-1}$ for W-dominant and W_2B-dominant materials respectively. The resulting thermal stress resistance also degrades in a similar manner, and is lower for both materials compared to pure W. Although it should be noted that thermal stress resistance will likely improve with increasing temperature for the W_2B-dominant material, which opposes the case for pure W.

Overall, the results indicate a trade-off in performance between shielding and thermal–mechanical properties with increasing W_2B content. The trade-off must be quantitatively treated through the development of a shielding figure of merit, which will be performed in future work. It is also important to determine the boron chemistry more accurately in the samples post-sintering and to assess their irradiation damage tolerance.

CRediT authorship contribution statement

Samuel Humphry-Baker: Conceptualization, Supervision, Investigation, Formal analysis, Funding acquisition, Writing – original draft. **Ouguzi Aihemaiti:** Investigation, Formal analysis, Writing – original draft. **Eugene Ivanov:** Conceptualization, Supervision, Writing – review & editing. **Eduardo del Rio:** Investigation, Formal analysis. **Colin Windsor:** Investigation, Formal analysis, Software. **Jack Astbury:** Supervision, Writing – review & editing.

Declaration of Competing Interest

The authors declare that they have no known competing financial interests or personal relationships that could have appeared to influence the work reported in this paper.

Data availability

Data will be made available on request.

Acknowledgements

This work is supported by the UK Engineering and Physical Sciences Research Council (EPSRC) Open Fellowship [Grant number EP/W008025/1].

References

[1] C.G. Windsor, J.G. Morgan, P.F. Buxton, Heat deposition into the superconducting central column of a spherical tokamak fusion plant, Nucl. Fusion. 55 (2) (2015) 023014.

[2] S.A. Humphry-Baker, G.D. Smith, Shielding materials in the compact spherical tokamak, Phil. Trans. R. Soc. A 377 (2019) 20170443.
[3] R. Prokopec, D.X. Fischer, H.W. Weber, M. Eisterer, Suitability of coated conductors for fusion magnets in view of their radiation response, Supercond. Sci. Technol. 28 (2014), 014005.
[4] D.X. Fischer, R. Prokopec, J. Emhofer, M. Eisterer, The effect of fast neutron irradiation on the superconducting properties of REBCO coated conductors with and without artificial pinning centers, Supercond. Sci. Technol.. 31 (2018), 044006.
[5] S.J. Zinkle, A. Quadling, Extreme materials environment of the fusion "fireplace", MRS Bull. (2022) https://doi.org/10.1557/s43577-022-00453-9.
[6] S. Kobayashi, N. Hosoda, R. Takashima, Tungsten alloys as radiation protection materials, Nucl. Instrum. Methods Phys. Res., Sect. A 390 (1997) 426–430, https://doi.org/10.1016/S0168-9002(97)00392-6.
[7] E.M. Duchnowski, R.F. Kile, L.L. Snead, J.R. Trelewicz, N.R. Brown, Reactor performance and safety characteristics of two-phase composite moderator concepts for modular high temperature gas cooled reactors, Nucl. Eng. Des. 368 (2020), 110824.
[8] T. Hayashi, K. Tobita, Y. Nakamori, S. Orimo, Advanced neutron shielding material using metal hydride and borohydride, in: France, 2007.
[9] S.X. Oliver, M.L. Jackson, P.A. Burr, Radiation-induced evolution of tungsten carbide in fusion reactors: accommodation of defect clusters and transmutation elements, ACS Appl. Energy Mater. 3 (2019) 868–878, https://doi.org/10.1021/acsaem.9b01990.
[10] Colin G. Windsor, Jack O. Astbury, James J. Davidson, Charles J.R. McFadzean, J. Guy Morgan, Christopher L. Wilson, Samuel A. Humphry-Baker, Tungsten boride shields in a spherical tokamak fusion power plant, Nucl. Fusion. 61 (8) (2021) 086018.
[11] D. Zhang, P. Richardson, M. Wang, H. Tu, C. Li, L. He, H. Zhang, L. Shi, Synthesis, microstructure, and formation mechanism of a potential neutron shielding material: WAlB, J. Mater. Sci. Technol. 126 (2022) 127–131, https://doi.org/10.1016/j.jmst.2022.03.013.
[12] K.A. Khor, L.G. Yu, G. Sundararajan, Formation of hard tungsten boride layer by spark plasma sintering boriding, Thin Solid Films 478 (1-2) (2005) 232–237.
[13] M.S. Koval'chenko, L.G. Bodrova, E.K. Fen', Densification kinetics of higher molybdenum and tungsten borides in hot pressing, Powder Metall Met Ceram. 14 (6) (1975) 469–473.
[14] Ke Ma, Xiaozhou Cao, Xiangxin Xue, Mechanical properties, microstructure and grain orientation of hot pressed WB2 ceramics with Co as a sintering additive, Ceram. Int. 45 (12) (2019) 14718–14727.
[15] J. Qiao, Q. Zhang, Y. Zhou, X. Gao, G. Wu, Microstructure and properties of WB/Al nuclear shielding composites prepared by spark plasma sintering, Ceram. Int. 48 (2022) 31952–31964, https://doi.org/10.1016/j.ceramint.2022.07.131.
[16] J.M. Marshall, D. Walker, P.A. Thomas, HRXRD study of the theoretical densities of novel reactive sintered boride candidate neutron shielding materials, Nucl. Mater. Energy. 22 (2020), 100732.
[17] J.M. Marshall, F. Tang, Y. Han, P.A.J. Bagot, M.P. Moody, Multi-Scale microscopy of Reactive sintered boride (RSB) neutron shielding materials, Nucl. Mater. Energy 33 (2022), 101285, https://doi.org/10.1016/j.nme.2022.101285.
[18] G.V. Samsonov, The phases of the tungsten–boron system, in: Doklady Akademii Nauk, Russian Academy of Sciences, 1957: pp. 1299–1301.
[19] K.I. Portnoi, V.M. Romashov, Yu.V. Levinskii, I.V. Romanovich, Phase diagram of the system tungsten-boron, Soviet Powder Metall. Metal Ceram. 6 (5) (1967) 398–402.
[20] Q. Gu, G. Krauss, W. Steurer, Transition metal borides: superhard versus ultra-incompressible, Adv. Mater. 20 (2008) 3620–3626.
[21] Reza Mohammadi, Andrew T. Lech, Miao Xie, Beth E. Weaver, Michael T. Yeung, Sarah H. Tolbert, Richard B. Kaner, Tungsten tetraboride, an inexpensive superhard material, Proc. Natl. Acad. Sci. U.S.A. 108 (27) (2011) 10958–10962.
[22] U.K. Vashi, R.W. Armstrong, G.E. Zima, The hardness and grain size of consolidated fine tungsten powder, Metall. Trans. 1 (6) (1970) 1769–1771.
[23] Z. Qin, W. Gong, X. Song, M. Wang, H. Wang, Q. Li, Effect of pressure on the structural, electronic and mechanical properties of ultraincompressible W_2B, (2018).
[24] Alexander G. Kvashnin, Hayk A. Zakaryan, Changming Zhao, Yifeng Duan, Yulia A. Kvashnina, Congwei Xie, Huafeng Dong, Artem R. Oganov, New tungsten borides, their stability and outstanding mechanical properties, J. Phys. Chem. Lett. 9 (12) (2018) 3470–3477.
[25] Y. Mutoh, K. Ichikawa, K. Nagata, M. Takeuchi, Effect of rhenium addition on fracture toughness of tungsten at elevated temperatures, J. Mater. Sci. 30 (3) (1995) 770–775.
[26] A.V. Babak, E.I. Uskov, Methodological aspects of studying the fracture toughness of tungsten. Report No. 2, Strength Mater 16 (7) (1984) 943–949.
[27] The high temperature compressive behaviour of ZrCp/W composites and the strengthening mechanisms, PhD Thesis, Harbin Institute of Technology, 2008.
[28] M.M. Gauthier, Engineered materials handbook, ASM International, 1995.
[29] M. Athanasakis, E. Ivanov, E. del Rio, S.A. Humphry-Baker, A high temperature W2B–W composite for fusion reactor shielding, J. Nucl. Mater. 532 (2020), 152062, https://doi.org/10.1016/j.jnucmat.2020.152062.
[30] Y. Lin, C. McFadzean, S.A. Humphry-Baker, Oxidation resistance of WB and W2B-W neutron shields, J. Nucl. Mater. 565 (2022), 153762, https://doi.org/10.1016/j.jnucmat.2022.153762.
[31] C.J. Werner, J.S. Bull, C.J. Solomon, F.B. Brown, G.W. McKinney, M.E. Rising, D.A. Dixon, R.L. Martz, H.G. Hughes, L.J. Cox, A.J. Zukaitis, J.C. Armstrong, R.A. Forster, L. Casswell, MCNP Version 6.2 Release Notes, Los Alamos National Lab. (LANL), Los Alamos, NM (United States), 2018. https://doi.org/10.2172/1419730.
[32] C1421_16 Standard Test Methods for Determination of Fracture Toughness of Advanced Ceramics at Ambient Temperature, (2016).
[33] P.L. Raffo, L.F. Hehemann, Grain growth in dilute tungsten-boron alloys, NATIONAL AERONAUTICS AND SPACE ADMINISTRATION CLEVELAND OH LEWIS RESEARCH CENTER, 1965.
[34] Hong Li, R.C. Bradt, The effect of indentation-induced cracking on the apparent microhardness, J. Mater. Sci. 31 (4) (1996) 1065–1070.
[35] E. Lassner, W.-D. Schubert, Tungsten, Springer, US, Boston, MA, 1999 http://link.springer.com/10.1007/978-1-4615-4907-9 (accessed November 20, 2015.
[36] H.C. Lee, J. Gurland, Hardness and deformation of cemented tungsten carbide, Mater. Sci. Eng. 33 (1) (1978) 125–133.
[37] E. Mazhnik, A.R. Oganov, A model of hardness and fracture toughness of solids, J. Appl. Phys. 126 (2019), 125109.
[38] William G. Fahrenholtz, Gregory E. Hilmas, Inna G. Talmy, James A. Zaykoski, Refractory diborides of zirconium and hafnium, J. Am. Ceram. Soc. 90 (5) (2007) 1347–1364.
[39] D.-W. Ni, G.-J. Zhang, Y.-M. Kan, P.-L. Wang, Hot pressed HfB2 and HfB2–20 vol% SiC ceramics based on HfB2 powder synthesized by borothermal reduction of HfO2, Int. J. Appl. Ceram. Technol. 7 (2010) 830–836.
[40] Y. Liu, X. Liu, C. Lai, J. Ma, X. Meng, L. Zhang, G. Xu, Y. Lu, H. Li, J. Wang, S. Chen, Boriding of tungsten by the powder-pack process: Phase formation, growth kinetics and enhanced neutron shielding, Int. J. Refract Metal Hard Mater. 110 (2023), 106049, https://doi.org/10.1016/j.ijrmhm.2022.106049.
[41] Gui-Ming Song, Yu-Jin Wang, Yu Zhou, The mechanical and thermophysical properties of ZrC/W composites at elevated temperature, Mater. Sci. Eng. A 334 (1-2) (2002) 223–232.
[42] T. Zhang, Y. Wang, Y. Zhou, T. Lei, G. Song, Compressive deformation behavior of a 30 vol.% ZrC p/W composite at temperatures of 1300–1600 deg. C, Mater. Sci. Eng.. A, Struct. Mater.: Properties, Microstruct. Process. 474 (2008) 382–389.
[43] Dmytro Demirskyi, Ievgen Solodkyi, Toshiyuki Nishimura, Yoshio Sakka, Oleg Vasylkiv, High-temperature strength and plastic deformation behavior of niobium diboride consolidated by spark plasma sintering, J. Am. Ceram. Soc. 100 (11) (2017) 5295–5305.
[44] Eric W. Neuman, Gregory E. Hilmas, William G. Fahrenholtz, A. Dominguez-Rodriguez, Strength of Zirconium Diboride to 2300°C, J. Am. Ceram. Soc. 96 (1) (2013) 47–50.
[45] T. Palacios, M.A. Monge, J.Y. Pastor, Tungsten–vanadium–yttria alloys for fusion power reactors (I): Microstructural characterization, Int. J. Refract Metal Hard Mater. 54 (2016) 433–438.
[46] T. Shen, Y. Dai, Y. Lee, Microstructure and tensile properties of tungsten at elevated temperatures, J. Nucl. Mater. 468 (2016) 348–354, https://doi.org/10.1016/j.jnucmat.2015.09.057.
[47] W.H. Rhodes, E.V. Clougherty, D. Kalish, Research and development of refractory oxidation-resistant diborides. Part II. Volume IV. Mechanical properties. Technical report, 15 September 1967–15 May 1969., MANLABS, INC., CAMBRIDGE, MASS., 1970.
[48] Y.S. Touloukian, R.W. Powell, C.Y. Ho, P.G. Klemens, Thermophysical properties of matter-the tprc data series. volume 1. thermal conductivity-metallic elements and alloys, Thermophysical and Electronic Properties Information Analysis Center Lafayette In, 1970.
[49] T. Tanabe, C. Eamchotchawalit, C. Busabok, S. Taweethavorn, M. Fujitsuka, T. Shikama, Temperature dependence of thermal conductivity in W and W-Re alloys from 300 to 1000 K, Mater. Lett. 57 (19) (2003) 2950–2953.
[50] M. Fukuda, A. Hasegawa, S. Nogami, Thermal properties of pure tungsten and its alloys for fusion applications, Fusion Eng. Des. 132 (2018) 1–6.
[51] M. Fujitsuka, B. Tsuchiya, I. Mutoh, T. Tanabe, T. Shikama, Effect of neutron irradiation on thermal diffusivity of tungsten–rhenium alloys, J. Nucl. Mater. 283–287 (2000) 1148–1151, https://doi.org/10.1016/S0022-3115(00)00170-7.
[52] L.N. Larikov, Y.F. Yurchenko, Structure and Properties of Metals and Alloys, Naukova Dumka, Kiev, 1985.
[53] A.V. Blinder, A.S. Bolgar, Specific heat and enthalpy of borides of transition metals in a wide temperature range, Poroshk. Metall. 72–76 (1991).
[54] D. Hasselman, Thermal Stress Resistance of Engineering Ceramics, Mater. Sci. Eng. 71 (1985) 251–264.
[55] Changming Zhao, Yifeng Duan, Jie Gao, Wenjie Liu, Haiming Dong, Huafeng Dong, Dekun Zhang, Artem R. Oganov, Unexpected stable phases of tungsten borides, Phys. Chem. Chem. Phys. 20 (38) (2018) 24665–24670.
[56] X.-Y. Cheng, X.-Q. Chen, D.-Z. Li, Y.-Y. Li, Computational materials discovery: the case of the W-B system, Acta Crystallographica Section C, Struct. Chem. 70 (2014) 85–103.
[57] Yongcheng Liang, Zheng Zhong, Wenqing Zhang, A thermodynamic criterion for designing superhard transition-metal borides with ultimate boron content, Comput. Mater. Sci 68 (2013) 222–228.
[58] E. Zhao, J. Meng, Y. Ma, Z. Wu, Phase stability and mechanical properties of tungsten borides from first principles calculations, Physical Chemistry Chemical Physics, PCCP. 12 (2010) 13158–13165.
[59] B. Paul, Prediction of elastic constants of multi-phase materials, BROWN UNIV PROVIDENCE RI, 1959.